# Nucleation, Growth, and Repair of a Cobalt-Based Oxygen Evolving Catalyst

Yogesh Surendranath, Daniel A. Lutterman, Yi Liu, and Daniel G. Nocera*

Department of Chemistry, 6-335, Massachusetts Institute of Technology, Cambridge, Massachusetts 02139-4307, United States

S *Supporting Information*

ABSTRACT: The mechanism of nucleation, steady-state growth, and repair is investigated for an oxygen evolving catalyst prepared by electrodeposition from Co^{2+} solutions in weakly basic electrolytes (Co-OEC). Potential step chronoamperometry and atomic force microscopy reveal that nucleation of Co-OEC is progressive and reaches a saturation surface coverage of ca. 70% on highly oriented pyrolytic graphite substrates. Steady-state electrodeposition of Co-OEC exhibits a Tafel slope approximately equal to $2.3 \times RT/F$. The electrochemical rate law exhibits a first order dependence on Co^{2+} and inverse orders on proton (third order) and proton acceptor, methylphosphonate (first order for $1.8\ mM \leq [MeP_i] \leq 18\ mM$ and second order dependence for $32\ mM \leq [MeP_i] \leq 180\ mM$). These electrokinetic studies, combined with recent XAS studies of catalyst structure, suggest a mechanism for steady state growth at intermediate MeP_i concentration $(1.8-18\ mM)$ involving a rapid solution equilibrium between aquo Co(II) and Co(III) hydroxo species accompanied with a rapid surface equilibrium involving electrolyte dissociation and deprotonation of surface bound water. These equilibria are followed by a chemical rate-limiting step for incorporation of Co(III) into the growing cobaltate clusters comprising Co-OEC. At higher concentrations of MeP_i $([MeP_i] \geq 32\ mM)$, $MePO_3^{2-}$ equilibrium binding to Co(II) in solution is suggested by the kinetic data. Consistent with the disparate pH profiles for oxygen evolution electrocatalysis and catalyst formation, NMR-based quantification of catalyst dissolution as a function of pH demonstrates functional stability and repair at pH values >6 whereas catalyst corrosion prevails at lower pH values. These kinetic insights provide a basis for developing and operating functional water oxidation (photo)anodes under benign pH conditions.
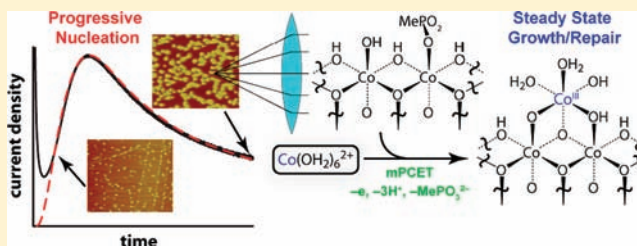
INTRODUCTION

The electrochemical splitting of water into hydrogen and oxygen is a high energy density method for storing solar energy in the form of chemical fuels.[1-4] This endergonic electrochemical conversion stores 1.23 V and consists of the four electron, four proton oxidation of water to oxygen and the reduction of the produced protons to hydrogen. Of these two half-reactions, the oxygen evolution reaction (OER) is particularly demanding because it requires the coupling of multiple proton and electron transfers,[5-7] the distribution of four redox processes over a narrow potential range, and the formation of two oxygen–oxygen bonds.[8-14] The efficiency and conditions required for this reaction are key determinants of the overall viability of energy storage via water-splitting,[4] and accordingly, the continued development of effective OER catalysts[15-34] stands as a central scientific and technological challenge in energy conversion.

We have emphasized the development of inexpensive, highly manufacturable water-splitting catalysts that may be easily integrated with photovoltaic substrates. The simple operation of the catalyst from conventional water sources under benign conditions is an important step toward providing distributed solar energy storage at low-cost.[35] We have recently described the self-assembly of a highly active cobalt-based oxygen evolving catalyst that forms as a thin film when aqueous solutions of Co^{2+} salts are electrolyzed in the presence of phosphate (Co–P_i), borate (Co–B_i), or methylphosphonate (Co–MeP_i) (collectively termed Co-OEC);[36,37] more recently, we have used a similar strategy to prepare a Ni–B_i catalyst.[38] These catalysts are of interest because they (1) form *in situ* under mild conditions on a variety of conductive substrates;[36-39] (2) exhibit high activity in pH 7–9 water at room temperature;[36,37] (3) are functional in impure water;[37,39] (4) are composed of inexpensive, earth-abundant materials;[36,37] (5) self-heal by reversing catalyst corrosion at open circuit upon application of a potential;[40] (6) are functional models of the oxygen-evolving complex of Photosystem II;[41] and (7) can be interfaced with light absorbing and charge separating materials.[42-48] The ability to perform the latter under benign conditions has enabled the development of the artificial leaf.[49-51] In the architecture of the leaf, the Co-OEC is interfaced to a Si junction in a wireless configuration to allow for the direct splitting of water under illumination with 1 sun of AM 1.5 simulated sunlight.

In developing photoelectrochemical and photovoltaic-based architectures for water splitting, such as the artificial leaf, attention must be paid to the (semi)conductor|catalyst|

electrolyte interface where efficiency determining processes such as photovoltage generation, current rectification, light transmission, and catalysis must take place simultaneously. Accordingly, the continued development and improvement of devices such as the artificial leaf provide an imperative for understanding catalyst deposition and morphology of the catalyst on surfaces so as to permit synthetic control over the microstructure of the (semi)conductor|catalyst| electrolyte interface.[42,43,52,53] Such studies of Co-OEC are enabled by the ability to form Co-OEC at potentials significantly lower than that required for OER. We now report mechanistic details of the pathway for catalyst nucleation and steady-state growth, and its relationship to catalyst repair processes. The progressive nature of the nucleation process of Co-OEC has been isolated by using chronoamperometry and AFM imaging. In addition, hydrodynamic electrokinetic methods have been employed to furnish the rate law for steady-state catalyst growth, and the pH regimes of functional catalyst stability and repair have been defined from electrokinetic profiles. These kinetic insights provide a coherent picture of the electrodeposition process of Co-OEC and provide a rational framework for refining the properties of the (semi)conductor|catalyst|solution interface for the development of improved devices such as the artificial leaf.

■ RESULTS

To probe the initial stages of catalyst formation, chronoamperograms of freshly polished glassy carbon electrodes were recorded in quiescent solutions of Co^{2+} (0.4 mM) containing 0.02 M MePi and 1.97 M KNO_3 electrolyte (pH 7.5). We note that an active OER catalyst may be electrodeposited from solutions containing phosphate or borate electrolytes.[36,37,54] For the studies reported here, methylphosphonate (MePi) was chosen as the electrolyte for catalyst growth, as opposed to phosphate or borate, because low millimolar concentrations of Co^{2+} are indefinitely stable and no discernible precipitate is observed in solution over days. In the case of Pi or Bi, precipitate will form over the course of several hours. Notwithstanding, the results reported here are generalizable as previous studies have shown that the nature of the catalyst is the same whether electrodeposition proceeds from Pi, Bi, or MePi.[37] The chronoamperograms of this solution are shown in Figure 1 along with a slow scan (5 mV/s) cyclic voltammogram (CV) recorded under identical conditions. The CV exhibits an anodic wave at 0.99 V (all potentials are referenced to the normal hydrogen electrode (NHE)) characteristic of catalyst formation. Following initial polarization at 0.75 V (omitted in Figure 1), during which time only double-layer charging occurred, the electrode potential was stepped to various voltages spanning the catalyst formation wave in the CV. At all the step potentials explored, the chronoamperograms display three features. The current rapidly decays from an initial spike immediately following the potential step followed by a rapid rise to attain a peak followed by a gradual decay toward a nonzero limiting value. For higher potentials, the magnitude of the peak current density, j_{max}, systematically increases whereas the time corresponding to the peak, t_{max}, systematically decreases.

To further interrogate the nucleation process, partially nucleated catalyst films were imaged by atomic force microscopy (AFM). Potential step chronoamperograms were recorded using highly oriented pyrolytic graphite (HOPG) working electrodes cleaved from a bulk slab prior to the experiment; details of the electrode preparation are provided in
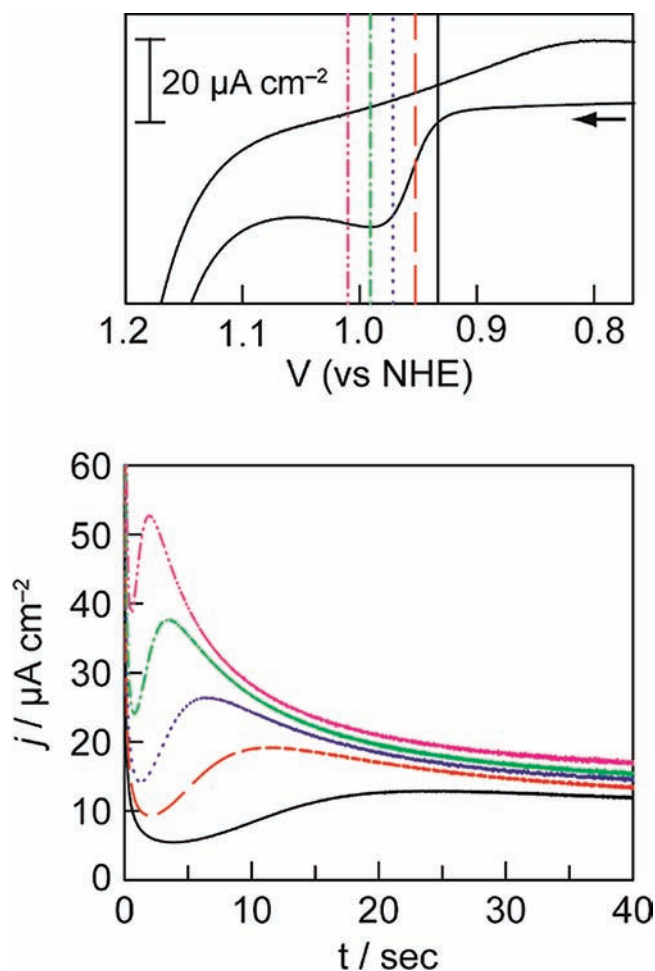
Figure 1. (top) Cyclic voltammogram (scan rate = 5 mV/s) and (bottom) potential step chronoamperograms of a freshly polished glassy carbon disk electrode in 0.4 mM Co^{2+}, and 0.02 M MePi, 1.97 M KNO_3 electrolyte at pH 7.5. Chronoamperometry data recorded with a step voltage of 1.01 (magenta, —··), 0.99 (green, —·—·), 0.97 (blue, ···), 0.95 (red, – – –), and 0.93 V (black, —) following a 100 s pulse at 0.75 V (not shown). Step voltages used to collect chronoamperograms are indicted with vertical lines overlaid on the CV trace.

the Supporting Information. Similar to the behavior observed using a glassy carbon working electrode, potential step polarization from 0.75 to 0.97 V in 0.4 mM Co^{2+}, 0.02 M MePi, and 1.97 M KNO_3 electrolyte (pH 7.5) leads to a nucleated growth trace with $t_{max} = 10.1(1)$ s. Using these same conditions, an array of catalyst-coated HOPG electrodes were prepared following potential step polarization that was ceased at ca. 0.2, 0.5, 1, 2, 4, and 8 × t_{max}. Following the termination of electrolysis, the electrodes were rinsed thoroughly with reagent grade water, dried, and imaged by AFM. Representative images are shown in Figures 2 and S2. The relatively smooth HOPG electrode surface is visible underneath discontinuous islands of Co-OEC. The bare HOPG surface is punctuated randomly by long lines due to step edges between graphite layers. Islands of catalyst are distributed randomly on the highly oriented pyrolytic graphite surface, excluding a higher density of islands that localize at step edges. At 0.2 × t_{max}, the island sizes range from 35 to 55 nm and catalyst covers 9(1)% of the surface. At 0.5 × t_{max}, the island sizes range from 65 to 85 nm, and catalyst surface coverage increases to 27(2)%. At 1 × t_{max}, catalyst
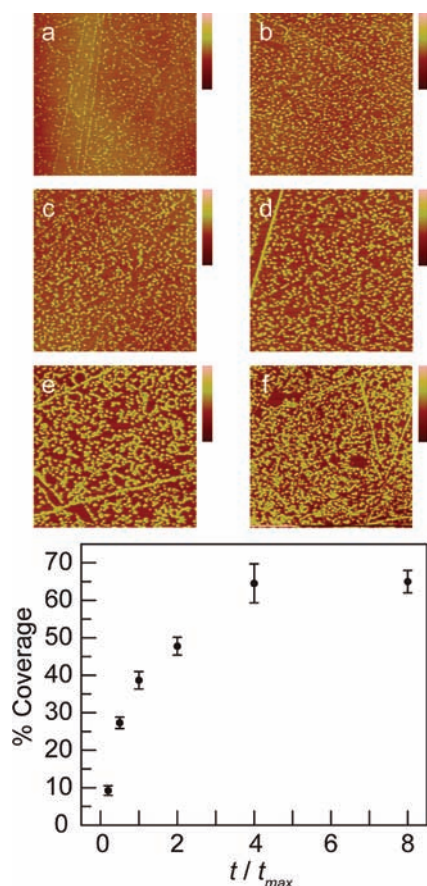
Figure 2. Representative 5×5 μm^2 AFM images of a highly oriented pyrolytic graphite electrode after being subjected to potential step polarization from 0.75 to 0.97 V for (a) 0.2, (b) 0.5, (c) 1, (d) 2, (e) 4, and (f) $8 \times t_{max}$ (=10.1(1) s). Bars to the right of each image indicate the depth with full scale values of (a) 20, (b) 30, (c) 50, (d) 75, (e) 75, and (f) 50 nm. Electrolyte conditions: 0.4 mM Co^{2+} and 0.02 M MeP_i, 1.97 M KNO_3 electrolyte at pH 7.5 (2 M ionic strength). Plot displays coverage percentage of catalyst versus the normalized duration of potential step polarization, t/t_{max}.

coverage rises to 39(2)%, and catalyst islands have begun to coalesce. Catalyst coverage continues to increase to 48(2)% at $2 \times t_{max}$ and 65(5)% at $4 \times t_{max}$, after which a plateau is reached at $8 \times t_{max}$ (65(3)%.) At $8 \times t_{max}$, the agglomerated catalyst islands range in size from 70 to 140 nm. The saturation behavior of the surface coverage of catalyst is clearly apparent from the plot of percent catalyst coverage versus t/t_{max} (Figure 2). Beyond $0.5 \times t_{max}$, a marked increase in particle number density does not accompany the further increase in surface coverage.

In order to deconvolute steady-state catalyst growth kinetics from nucleation kinetics, the following studies of catalyst growth were all conducted on preformed catalyst films exhibiting saturation surface coverage. Specifically, prior to the collection of steady-state kinetic data, a 200 s galvanostatic pulse at 50 $\mu A/cm^2$ was applied to the electrode, rotated at 2500 rpm. This pulse corresponds to 10 mC/cm^2 charge passed for catalyst deposition, which is ~10 fold higher than the typical charge passed at $8 \times t_{max}$ (<1 mC/cm^2) in the nucleated growth studies described above. This ensures that the catalyst film completely covers the surface of the Pt electrode and that the subsequent kinetic data is not influenced by nucleation processes. Using preformed 10 mC/cm^2 catalyst films as a substrate for steady-state catalyst growth, current densities for

catalyst formation from 0.4 mM Co^{2+}, 0.02 M MeP_i, and 1.97 M KNO_3 electrolyte (pH 7.5) were measured at a variety of rotation rates, ω, and applied potentials. For each potential examined, a Koutecký–Levich plot of j^{-1} versus $\omega^{-1/2}$ (Figure S3) was extrapolated to infinite rotation rate ($\omega^{-1/2} = 0$) to determine the activation controlled current density for catalyst formation, j_{ac}, in the absence of mass-transport limitations.[55] For all data points, ohmic potential losses amounted to <1 mV and were ignored. A Tafel plot of the applied potential versus the log of j_{ac} is shown in Figure 3. The data points exhibit linearity over 0.12 V and a slope of 60 mV/decade.
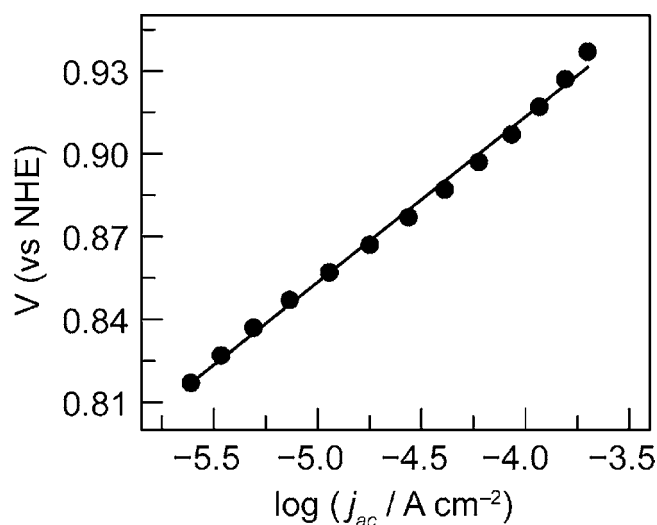

Figure 3. Tafel plot of Co-OEC catalyst film formation from 0.4 mM Co^{2+} and 0.02 M MeP_i, 1.97 M KNO_3 electrolyte at pH 7.5 onto a Pt rotating disk electrode. Activation controlled current density values (j_{ac}) were derived from Koutecký–Levich analysis of steady-state current densities measured at multiple rotation rates (Figure S3). The Tafel slope is 60 mV/decade.

The dependence of the catalyst formation rate on Co^{2+} concentration was interrogated by collecting Tafel plots of steady-state growth of catalyst using the procedure described above. Figure S4 shows these Tafel plots for catalyst growth from solutions containing $[Co^{2+}]$ = 0.1, 0.18, 0.32, 0.56, and 1 mM and 0.02 M MeP_i and 1.97 M KNO_3 (pH 7.5). The Tafel plot exhibits linearity over >1.5 decades in activation controlled current density and an average Tafel slope of 62(8) mV/decade. Interpolation of these Tafel plots at 0.84, 0.86, 0.88, and 0.90 V yields steady-state activation controlled current densities for catalyst growth as a function of Co^{2+} concentration (Figure 4). The data exhibit linearity over the decade range of Co^{2+} concentrations with an average slope of 1.1(1). These results establish that the electrodeposition process is first order in Co^{2+}.

The role of proton activity on the electrodeposition rate was defined from constructing Tafel plots over the pH range 7– 8.25 (Figure S5). Because acid is generated during catalyst formation and the buffer capacity was low, concentrated KOH was periodically added to maintain the bulk solution pH to within 0.02 pH units for the duration of Tafel data collection (see SI). All Tafel plots exhibit linearity over ~2 decades in activation controlled current density and an average Tafel slope of 60(4) mV/decade (Figure S5). Unlike the case described above for variations in the Co^{2+} concentration, the Tafel plots in Figure S5 are distributed dramatically in potential preventing
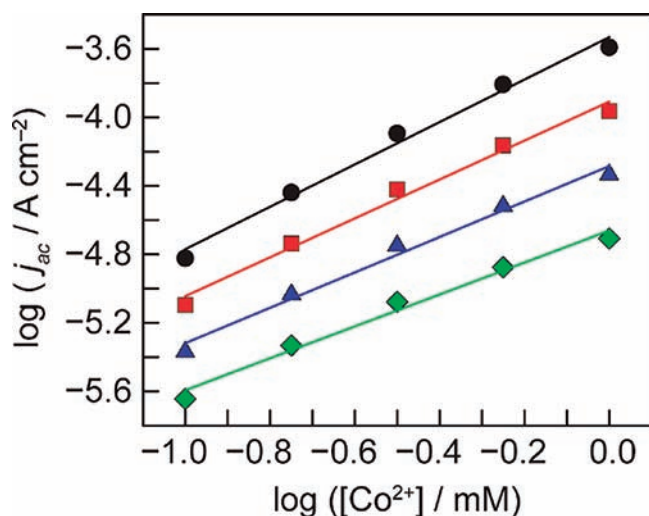
Figure 4. $[Co^{2+}]$ dependence of steady-state activation controlled current density for catalyst film formation in 0.02 M MeP_i, 1.97 M KNO_3 electrolyte at pH 7.5 (2 M ionic strength) at $E = 1.04$ (green ◆), 1.06 (blue ▲), 1.08 (red ■), and 1.1 V (black ●). Average slope is 1.1(1). Data were interpolated from Tafel plots in Figure S4.

a straightforward interpolation at constant potential over the entire pH range. However, interpolation of these Tafel plots at $j_{ac} = 3.2$, 10, 32, and 100 $\mu A/cm^2$ (log $(j_{ac}/A/cm^2) = -5.5$, -5, -4.5, and -4 on Figure S5) yields the required potential as a function of pH (Figure 5). The data are linear over the 1.25 pH
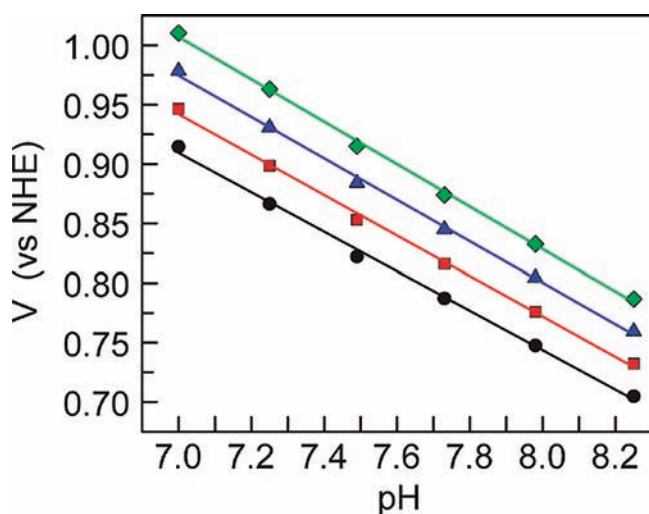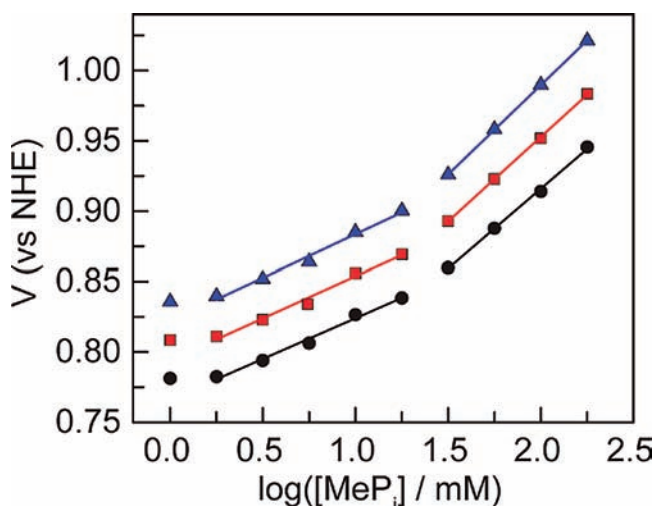

Figure 5. pH dependence of the potential for catalyst film formation in 0.4 mM Co^{2+} and 0.02 M MeP_i, 1.97 M KNO_3 electrolyte at $j_{ac} = 3.2$ (black ●), 10 (red ■), 32 (blue ▲), and 100 (green ◆) $\mu A/cm^2$. Average slope is $-172(5)$ mV/pH unit. Data were interpolated from Tafel plots in Figure S5.

unit range explored here and exhibit an average slope of $-172(5)$ mV/pH unit. In this experiment, the Tafel data were interpolated at constant current density, j_{ac}, and therefore, the potential dependence of the current density (the Tafel behavior) is convoluted with the slope of the potential versus pH plot.[56] Specifically

$$\left(\frac{\partial E}{\partial pH}\right)_j = -\left(\frac{\partial E}{\partial \log(j)}\right)_{pH}\left(\frac{\partial \log(j)}{\partial pH}\right)_E \quad (1)$$

Thus, the $-172(5)$ mV/pH unit slope observed in Figure 5, when divided by negative of the 60(4) mV/decade Tafel slope, yields the reaction order in pH of 2.9(2). Thus, these data establish third order dependence on pH and, therefore, inverse third order dependence on proton activity.

The dependence of the electrodeposition rate on the concentration of the proton-accepting electrolyte species was ascertained by collecting Tafel plots in 0.4 mM Co^{2+} (pH 7.5) over a MeP_i concentration range from 1 to 178 mM (Figure S6). All solutions contained sufficient KNO_3 background electrolyte to maintain a constant 2 M ionic strength. For each MeP_i concentration, Tafel data were collected using independently prepared 10 mC/cm^2 catalyst films and the bulk solution pH was maintained at 7.5 ± 0.02 with periodic addition of concentrated KOH (see SI). The Tafel data exhibit linearity over a ~2 decade range in current density and an average slope of 64(8) (Figure S6). Interpolation of these Tafel plots at $j_{ac} = 10$, 32, and 100 $\mu A/cm^2$ (log $(j_{ac}/A/cm^2) = -5$, -4.5, and -4 on Figure S6) yields the required potential as a function of the log of the MeP_i concentration (Figure 6). The

Figure 6. $[MeP_i]$ dependence of the potential for catalyst film formation in 0.4 mM Co^{2+} at pH 7.5 (2 M ionic strength with KNO_3 background electrolyte) at $j_{ac} = 10$ (black ●), 32 (red ■), and 100 (blue ▲) $\mu A/cm^2$. Average slopes are 60(2) and 120(7) mV/decade for the low and high buffer strength regions, respectively. Data were interpolated from Tafel plots in Figure S6.

data exhibit two distinct linear regions. For MeP_i concentrations between 32 and 178 mM, a slope of 120(7) mV/decade is observed, whereas a slope of 60(2) mV/decade is observed for MeP_i concentrations between 1.8 and 17.8 mM. As encountered above, the data in Figure 6 correspond to constant j_{ac}, and thus, the potential dependence of the current density (the Tafel behavior) is convoluted with the slope of the potential versus log$([MeP_i])$ plot.[56] For this case

$$\left(\frac{\partial E}{\partial \log([MeP_i])}\right)_j = \left(\frac{\partial E}{\partial \log(j)}\right)_{[MeP_i]}\left(\frac{\partial \log(j)}{\partial \log([MeP_i])}\right)_E \quad (2)$$

Therefore, the 120(7) and 60(2) mV/decade slopes observed in Figure 6 correspond to reaction orders of $-1.9(3)$ and $-0.9(1)$. These results establish inverse first order and inverse second order dependence on MeP_i concentration over the

ranges 1.8−17.8 mM and 32−178 mM, respectively. Below 1.8 mM MeP$_i$, the potential appears to be invariant with buffer strength. However, activation controlled current density data could not be obtained below 1 mM MeP$_i$ because local and bulk pH changes at very low buffer strength caused drastic systematic errors in the extrapolation of Koutecký−Levich plots to infinite rotation rate. Thus, while there appears to be a region of zero order dependence below 1.8 mM MeP$_i$, the lack of data at very low buffer strength makes this assignment tenuous at best.

As catalyst dissolution is expected to be the microscopic reverse of the catalyst formation process, the kinetics of catalyst dissolution were also quantified over a wide pH range. For this study, a series of 100 mC/cm^2 catalyst films were prepared on fluorine−tin oxide (FTO) working electrodes by electro-deposition at 1.05 V from quiescent 0.1 M phosphate electrolyte (P$_i$), pH 7 solutions containing 0.5 mM Co^{2+}. Under these conditions, negligible water oxidation catalysis is observed. Thus, the 100 mC/cm^2 charge passed provides an accurate estimate of the Co content of the film, ∼1 μmol Co/cm^2. After film preparation, each electrode was rinsed with reagent grade water and operated for water oxidation at 1 and 0 mA/cm^2 in stirred electrolyte solutions of 0.04 M Britton−Robinson buffer (see SI for details) that contained no Co^{2+} ion. At various times over the course of one hour, aliquots of the electrolyte solution were removed from the working compart-ment of the electrolysis cell. The Co^{2+} concentration in each aliquot was determined by measuring the magnitude of Co^{2+}-induced paramagnetic line broadening of the ^{31}P NMR peak for inorganic phosphate and comparing to a standard curve (see SI and Figure S7). From these concentration measurements, the fraction of Co dissolved from the film versus time was calculated and is shown for pH 4 in Figure 7. For electrodes
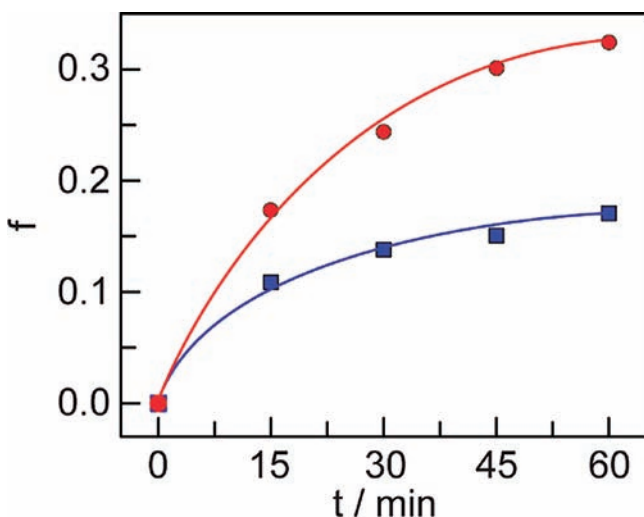
Figure 7. Fraction (*f*) of catalyst film dissolved versus time for an electrodes poised at 1 (blue ■) and 0 (red ●) mA/cm^2 in an initially Co^{2+}-free electrolyte solution of 0.04 M Britton−Robinson buffer, pH 4. Lines are presented to guide the eye.

operated at 0 and 1 mA/cm^2, catalyst corrosion prevails throughout the entire duration of the experiment. However, for the electrode held under open-circuit conditions (0 mA/cm^2), the rate of catalyst corrosion is greater than that for the electrode operated at 1 mA/cm^2. This is evidenced by both a greater fraction dissolved after 1 h for the former, 0.33, versus

the latter, 0.17, and a greater initial slope of the dissolution profile for the former. A similar phenomenon is also observed at pH 5 with a systematic decrease in the overall fraction dissolved after 1 h for both the 0 and 1 mA/cm^2 samples, but no dissolution is detected at pH 6 and 7. A plot of the total fraction, *f*, of Co dissolved after 1 h of electrolysis versus the solution pH is shown in Figure 8. This data establishes that Co-
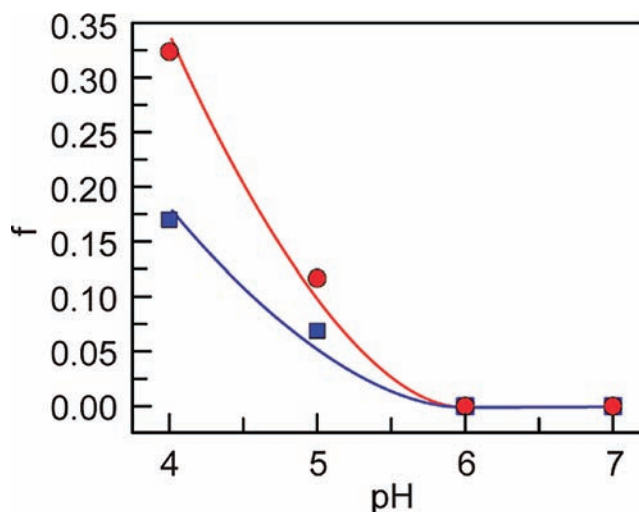
Figure 8. Fraction (*f*) of catalyst film dissolved after 1 h vs pH for electrodes poised at 1 (blue ■) and 0 (red ●) mA/cm^2 in 0.04 M Britton−Robinson buffer. Lines are presented to guide the eye.

OEC exhibits functional stability at > pH 6 but is subject to progressive dissolution below this pH.

■ DISCUSSION

Chronoamperometry affords valuable insight into the initial stages of catalyst formation. Important to these studies, a characteristic sharp anodic prefeature wave several hundred millivolts prior to the onset of water oxidation catalysis is observed in cyclic voltammograms of Co^{2+} in a buffering electrolyte at pH 7−9 (Figure 1).[36,37] A single CV scan of a freshly polished inert electrode with a switching potential beyond this prefeature wave but prior to the onset of catalysis is necessary and sufficient for the electrodeposition of a film active for water oxidation catalysis. We utilize this separation in potentials between water oxidation and catalyst formation to isolate the kinetics for catalyst formation.

Chronoamperograms with step potentials spanning the anodic prefeature wave (see Figure 1) reveal that the process is not merely a diffusion controlled oxidation of Co^{2+} ions. Whereas the potential step chronoamperogram of a electro-chemically and chemically reversible one-electron redox couple exhibits a simple decay of current proportional to $t^{-1/2}$ immediately following the potential step,[57] the chronoampero-grams of Co-OEC formation shown in Figure 1 are more complicated and reminiscent of the nucleated growth curves observed for the electrodeposition of metal films.[58] Following the potential step, the current decays rapidly from an initial spike due to currents associated with double-layer charging and adsorption/desorption events on the electrode surface.[58] This initial decay is followed by a rise in current that is attributed to the nucleation of the catalyst in the form of islands, which in effect serve to increase the surface area of the electrode. Quasi-three-dimensional growth of these catalyst islands gives rise to a

rapid increase in current until a maximum is reached. At this point, the reactant-depleted diffusion zones surrounding each growing catalyst island begin to overlap, causing the onset of semi-infinite linear diffusion of Co^{2+} ions and/or buffer constituents and an associated $t^{-1/2}$ decay of the current. Notably, at very long times, the current reaches a steady-state plateau rather than decaying to zero. This is attributed to convectional mass-transport of Co^{2+} to the surface at these long times. Importantly, the step potential has a marked impact on the time, t_{max}, and current density, j_{max}, at which the chronoamperogram exhibits its characteristic peak. Increasing the potential increases the driving force, and, thus, the rate of nucleation and catalyst growth, resulting in a systematic increase in j_{max}. The enhanced growth rate causes the diffusion fields to overlap more rapidly, and, consequently, leads to a systematic decrease in t_{max} with increasing driving force. Thus, control of the electrodeposition potential provides a convenient method for modulating t_{max} and j_{max}, enabling control over the surface coverage of catalyst islands with fidelity (vide infra). All of these characteristic features, together, establish that Co-OEC formation occurs via nucleation followed by diffusion limited growth.

Comparing the experimental chronoamperometric transients to theoretical predictions provides insight into the mechanism of nucleated growth, which can be characterized by one of two limiting extremes, progressive as opposed to instantaneous nucleation. In the instantaneous case, all potential nucleation sites, N_0, on the surface are assumed to give rise to nuclei at time zero following the potential step. In contrast, for the progressive case, the rate of nucleation is given by the following equation[59]

$$\frac{\partial N}{\partial t} = k_N \left(\frac{c}{c_0} \right)^n (N_0 - N) \qquad (3)$$

where k_N is the nucleation rate constant, and the term, $N_0 - N$, represents the number of unoccupied nucleation sites on the electrode surface. In eq 3, c and c_0 represent the local and bulk concentrations of all solution species upon which the nucleation rate depends, with the exponent, n, characterizing the overall reaction order. For the most elementary cases of instantaneous nucleation and progressive nucleation with a zero order nucleation rate law, $n = 0$, several theoretical models have been proposed to explain the chronoamperometric transient.[58,60,61] Additionally, for the case of progressive nucleation, a theoretical model has been elaborated to account for the influence of nonzero nucleation order on the expected chronoamperometric transient.[58] Distinguishing between the different mechanistic possibilities is most conveniently provided by comparing the theoretically predicted and experimental transients in a normalized form. In Figure 9, the experimental chronoamperometric transient for the 0.97 V step potential is plotted with the ordinate and abscissa normalized to the peak current density, $(j/j_{max})^2$, and peak time, (t/t_{max}), respectively. The normalized representation in Figure 9 serves to deconvolute changes in nucleation mechanism from changes in k_N and N_0 (eq 3) which are both substrate and potential dependent (vide supra). Overlaid on this normalized experimental data are three theoretical traces for the limiting cases of instantaneous nucleation followed by diffusion-limited growth[58] and progressive nucleation followed by diffusion-limited growth with the assumption of a zero order[58] and fourth order[59] nucleation rate law. Whereas other orders are
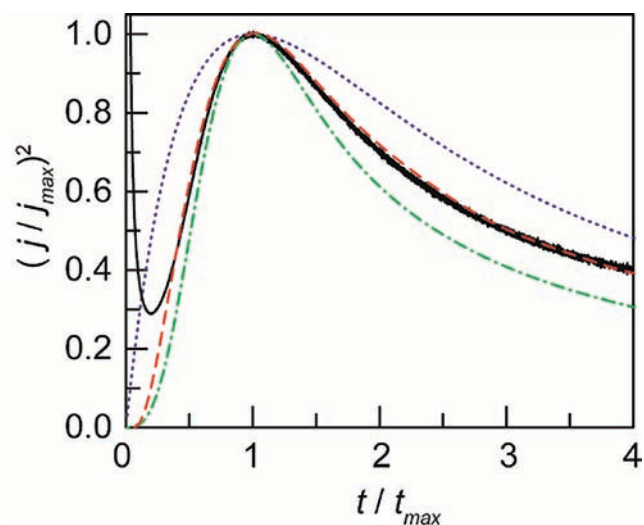
Figure 9. Normalized 0.97 V potential step chronoamperogram (black, —) of a freshly polished glassy carbon disk electrode 0.4 mM Co^{2+} and 0.02 M MeP$_i$, 1.970 M KNO_3 electrolyte at pH 7.5. Theoretical normalized chronoamperograms for the cases of instantaneous (blue, ⋯) nucleated growth and progressive nucleated growth with 0 (green, −·−·) and 4th (red, −−−) order nucleation rate laws.

possible, the point of Figure 9 is to show the differences between instantaneous and progressive nucleation and the impact of a nonzero order. The simulation of a fourth order rate law was chosen simply to represent qualitatively the deviations expected for a high, nonzero nucleation order and is not intended to quantitatively isolate the reaction order for nucleation. Given this limitation, Figure 9 clearly distinguishes between instantaneous and progressive nucleation. Instantaneous nucleation is characterized by a very sharp increase in current at early times and a broad peak, both of which are not observed in the experimental data. In contrast, the normalized experimental trace exhibits a slow rise, following double layer charging at early times, and a sharp peak, in agreement with that expected for zero order progressive nucleation. However, the experimental data deviates positively from theory for zero order progressive nucleation at times well beyond t_{max}. In contrast, the entire duration of the experimental transient is well modeled by the simulated curve for fourth order progressive nucleation except at early times. At early times, the current is dominated by non-Faradaic double-layer charging and adsorption/desorption events on the surface that are not accounted for by the theoretical models.[58,59] Good agreement between the experimental data and the theoretical trace is also observed for higher step potentials (1.01 and 0.99 V), but for the lower potential steps (0.95 and 0.93 V), the experimental current exhibits a positive deviation relative to the theory for long time points (Figure S1). In these cases, $t_{max} > 10$ s after the potential step, and thus, convective mass transport[62] is expected to elevate the current at long times relative to the theoretical models, which all assume purely diffusion-limited mass transport.[58,59] While this agreement between theory and experiment in Figure 9 is insufficient for determining a precise reaction order for the nucleation rate law, it does point to a progressive mechanism of nucleation with a nonzero order which is consistent with the complexity of the catalyst

formation process relative to simple metal film deposition and the third order rate law determined for steady-state film growth (vide infra).

Further evidence for the progressive nature of the nucleation process is afforded by AFM images of electrode surfaces subject to partial nucleation (Figure 2). To meet the stringent surface smoothness requirements of AFM, highly oriented pyrolytic graphite electrodes were employed. Consistent with the behavior predicted for high-order progressive nucleation,[59] the number of nuclei increase dramatically at early times, between 0.2 and $1 \times t_{max}$, after which relatively few new nuclei are formed. Instead, the already formed nuclei grow and coalesce to coat a greater proportion of the surface between 1 and $4 \times t_{max}$. The surface coverage plateaus after $4 \times t_{max}$ at ca. 65%. At this point, the diffusion fields of each growing catalyst island have completely overlapped thereby slowing the increase of surface coverage;[58] AFM shows that the tops of catalyst islands, which protrude into the undepleted bulk solvent, grow preferentially. We fully anticipate that prolonged electrolysis would lead to full surface coverage as the growing particles coalesce and form the continuous films observed by SEM in previous studies.[36,37,39] Although similar chronoamperometric transients are observed on different electrode substrates including glassy carbon (Figure 1), ITO, FTO, and HOPG, we expect that catalyst island morphology and surface coverage will depend on the nature of the electrode and its interaction with growing catalyst particles. Notwithstanding, these AFM results confirm that catalyst nucleation is progressive, and importantly, they point to a convenient method for patterning surfaces with catalyst islands. The appropriate choice of (photo)potential allows for control over the absolute value of t_{max} (vide supra), and termination of electrodeposition at the appropriate time relative to t_{max} provides a convenient handle with which to control the surface coverage of catalyst islands.

The growth of catalyst islands is subject to mass-transport limitations. In order to isolate the mechanistic details of catalyst growth, one must determine the current−potential relationship in the absence of mass-transport limitations and without influence from nucleation kinetics. To ensure the latter, steady state kinetic data were obtained by monitoring the rate of film deposition on electrodes on which catalyst was deposited after 10 mC/cm^2 was passed. This pretreatment of the electrode ensured complete coverage of the electrode surface with catalyst (vide supra), and therefore, the data should be negligibly impacted by nucleation and instead report on the kinetics of steady-state catalyst growth. Activation controlled current densities, j_{ac}, under any given set of potential and electrolyte conditions were obtained by extrapolating current densities measured at variable rotation rates on a rotating disk electrode (RDE) to infinite rotation speed (Figure S3).[57] A Tafel plot of the applied potential versus the log of j_{ac} exhibits good linearity over an ~2 decade range in activation-controlled current density and a slope of 60 mV/decade (Figure 3). A 60 mV/decade slope implies a catalyst formation mechanism involving a one-electron reversible equilibrium preceding a chemical rate-limiting step for catalyst formation.[56]

XAS studies have established that as-deposited Co-OEC catalyst films comprise molecular cobaltate clusters.[63] The clusters form by self-assembly following the oxidation of Co^{2+} to Co^{3+}. The reaction order in Co^{2+} is obtained directly from interpolation of Tafel plots collected at various Co^{2+} concentrations. Interpolation at constant applied potential yields j_{ac} as a function of the Co^{2+} concentration. As Figure 4

shows, a clear first order dependence is observed across a 60 mV range of potential values spanning the linear Tafel region. Taken together with the 60 mV/decade Tafel slope, this result implies that the reversible one-electron equilibrium step also involves a single Co^{2+} ion. This result shows that a mechanism involving multinuclear solution species is not required for catalyst self-assembly.

As the Co(aq)$^{2+/3+}$ redox couple is 1.92 V,[64] it is expected that one or more protons are involved in the one-electron oxidation of Co^{2+} to Co^{3+} and catalyst assembly. Insight into the number of protons exchanged in equilibrium prior to the rate limiting chemical step is provided by interpolation of pH dependent Tafel plots. Below pH 7, reliable data cannot be obtained because the deposition process begins to overlap with water oxidation thus convoluting the Tafel behavior. Above pH 8.25, the Tafel slope begins to rise significantly above 60 mV/decade thus preventing a straightforward interpretation of the reaction order. Hence Tafel data were collected over the pH range 7−8.25 (Figure S5). The potential versus pH plot of Figure 5 exhibits good linearity over the pH range explored for a 1.5 decade range of j_{ac} values. The slope of these plots, taken together with the 60 mV/decade Tafel slope, establishes an inverse third order dependence on proton activity. Given that the pK_a = 7.0 for MeP$_i$, under these ionic strength conditions (see SI for details of pK_a calculation at 2 M ionic strength), the concentration of MePO$_3{}^{2-}$ does not change in a logarithmic fashion over the range of pH interrogated here. Equilibria involving this species (vide infra), therefore, will not appreciably influence the apparent reaction order in proton. Taken together, these results suggest that the oxidation of Co^{2+} to Co^{3+} is coupled to three protons, which permits access to Co^{3+} at low potentials and accordingly enables catalyst self-assembly from solution.

The high degree of proton coupling to the reversible one-electron transfer establishes the key role for MeP$_i$ (or P$_i$ or B$_i$) as the proton acceptor in catalyst formation. The anion additionally has the proclivity to bind cobalt centers of nascent catalyst clusters. Interpolation of Tafel plots collected over a wide range of buffer strengths (1−178 mM) indicates that the potential required to sustain a given j_{ac} increases as buffer strength increases (Figure 6). The requirement for additional driving force with increasing buffer strength indicates an inhibitory effect of MeP$_i$ on the catalyst growth process. Furthermore, the potential versus log([MeP$_i$]) plot exhibits two distinct regions of different slopes, at buffer strengths beyond 32 mM (log([MeP$_i$]) = 1.5), a −120 mV/decade slope is observed corresponding to inverse second order dependence in MeP$_i$. At intermediate buffer strengths, 1.8−17.8 mM (log([MeP$_i$]) = 0.25−1.25), a −60 mV/decade slope is observed corresponding to inverse first order dependence in MeP$_i$. Importantly, the transition between inverse first and second order behavior corresponds well to the established binding constant for MeP$_i$ to Co^{2+} in solution.[65] At 50 mM MeP$_i$, 50% of the Co^{2+} in solution is estimated to be bound to MePO$_3{}^{2-}$ under the pH and ionic strength conditions of this study (see SI for details of binding calculation). This observation suggests that the observed inverse second order behavior at high buffer strength is due, in part, to MePO$_3{}^{2-}$ binding to Co^{2+} in solution. On the basis of phosphate binding constants,[66] protonated forms of MeP$_i$ are not expected to bind Co^{2+}, and the impact of these species on catalyst growth can be safely ignored. The underlying first order behavior, which spans 1.8−178 mM (log([MeP$_i$]) = 0.25−2.25) buffer strength, suggests a
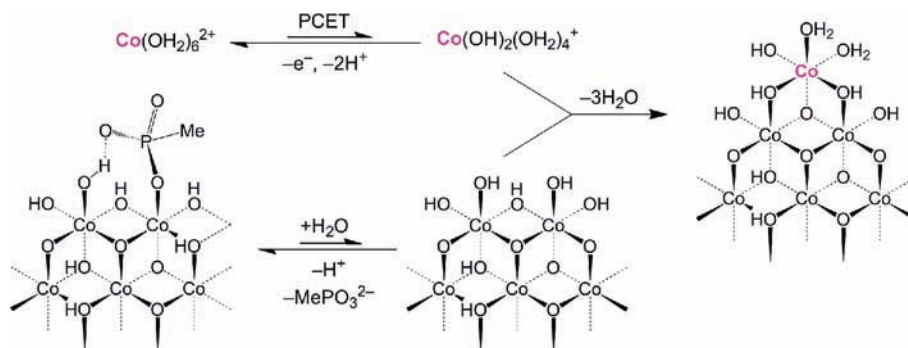
**Figure 10.** Proposed mechanism of Co-OEC catalyst film formation.

second mode of catalyst growth inhibition, which we attribute to MeP_i binding to clusters in the growing catalyst film. Thus, equilibrium dissociation of MeP_i from the surface must precede incorporation of newly oxidized Co centers.

The data in Figures 3−6 establish the following electrochemical rate law for the growth of Co-OEC catalyst films

$$j_{ac} = k_0([Co^{2+}])(a_{H^+})^{-3}([MeP_i])^{-1}\exp\left[\frac{FE}{RT}\right] \quad (4)$$

where k_0 is a potential-independent rate constant. This constant is proportional to the exchange current density for the electrodeposition process. The rate expression carries the observed first order dependence on $[Co^{2+}]$ (Figure 4), inverse third order dependence on proton activity, a_{H^+} (Figure 5), inverse first order dependence on $[MeP_i]$ at intermediate buffer strength (Figure 6), and the exponential relationship with potential, E (Figure 3). Rearrangement of the log form of eq 4 yields a Tafel slope, $\partial E/\partial\log(i)$, of 59 mV/decade that is also consistent with the experimental data shown in Figure 3.

The electrochemical rate law in eq 4 is consistent with the following mechanistic sequence:

$$A + \{Co^{2+}\} \rightleftharpoons B + \{Co^{3+}\} + e^- + 3H^+ + MeP_i \quad (5)$$

$$B + \{Co^{3+}\} \rightarrow C \quad (6)$$
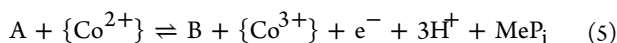
Here, a reversible one electron, three proton equilibrium is followed by a chemical rate limiting step for catalyst formation. In this sequence, A, B, and C designate surface species whereas Co ions in solution are given in brackets. The nature of the species is discussed below. This mechanistic sequence defined by eqs 5 and 6 implies that phase transfer of Co ions from solution to the film occurs as part of the rate-limiting step, a contention that is supported by the following kinetics analysis.

The velocity of the reaction, v, is given by

$$v = k_2\theta_B[\{Co^{3+}\}] \quad (7)$$

where k_2 is the rate constant for the chemical step, $[\{Co^{3+}\}]$ is the concentration of the $\{Co^{3+}\}$ species in solution, and θ_B is the surface coverage of the solid phase intermediate participating in the rate-limiting chemical transformation. In this formalism, θ_B is the surface concentration of B (Γ, in mol/cm^2) divided by the maximum surface concentration (Γ_{max}). We note that the number of active sites for film growth on the surface may represent a small proportion of the total number of solvent exposed Co centers in the film. Thus, Γ_{max} does not equal the number of exposed Co centers per cm^2, but rather the number of *active sites* for film growth per cm^2, and θ_B represents the fraction of these active sites in the form of intermediate B.

Similarly, θ_A represents the fraction of active sites for film growth in the form of intermediate A. As such, the ratio of $\theta_B \times [\{Co^{3+}\}]$ to the product of resting state species, $\theta_A \times [\{Co^{2+}\}]$, is given by the Nernst equation

$$\frac{\theta_B[\{Co^{3+}\}]}{\theta_A[\{Co^{2+}\}]} = K_1(a_{H^+})^{-3}([MeP_i])^{-1}\exp\left[\frac{FE}{RT}\right] \quad (8)$$

where K_1 is the equilibrium constant at $E = 0$. This equation represents a quasi-equilibrium assumption for the conversion described by eq 5. Substituting for $\theta_B \times [\{Co^{3+}\}]$ in eq 7 yields

$$v = \theta_A K_1 k_2([\{Co^{2+}\}])(a_{H^+})^{-3}([MeP_i])^{-1}\exp\left[\frac{FE}{RT}\right] \quad (9)$$

If the surface coverage of the resting state species, A, is appreciable (>0.9) over the potential and current range in which Tafel and other kinetic data are collected, θ_A will not vary appreciably with potential and can be set as a constant. Under these conditions, eq 9 approximates the experimental rate law, eq 4, with

$$k_0 = F \times \theta_A K_1 k_2 \quad (10)$$

Information about the structure of resting state species, A, is provided by X-ray absorption spectroscopy (XAS),[63] which reveals Co-OEC to be composed of Co-oxo/hydroxo clusters composed of edge-sharing CoO_6 octahedra, which are the basic structural components of the extended planes of alkali metal cobaltates, particularly Co(O)OH.[67] Within the framework of this structural model, it is reasonable to invoke that growth of the clusters, and thus, of the catalyst film itself proceeds via attachment of new Co fragments to the exposed edges of these clusters. Given that Co^{2+} binding to $MePO_3^{2-}$ cannot account for the inverse first order dependence on MeP_i at intermediate buffer strengths, these exposed edge sites are proposed to be coordinated to MeP_i buffering species in the resting state. This, taken together with the first pK_a of $Co(OH_2)_6^{2+}$ of 9.2 (see SI for details of calculation), establishes that $Co(OH_2)_6^{2+}$ is the resting-state species in solution.

Figure 10 shows a proposed mechanistic model for Co-OEC film growth that is consistent with the surface and solution resting-state species and the electrochemical rate law given by eq 4. A portion of the growing cobaltate cluster is shown to present the surface active sites from which growth may occur. In this mechanistic model, surface and solution phase reactions exist in equilibrium prior to the rate limiting phase transfer of Co to the growing catalyst surface. Given that the net reaction to form the catalyst consists of a three proton, one electron oxidation, Co^{2+} to Co(O)OH clusters, and that all of these

proton and electron transfers exist in equilibrium, we believe it is unlikely that phase transfer, which is expected to be irreversible, occurs prior to the completion of each equilibrium step. Thus, in solution, the $Co(OH_2)_6^{2+}$ is proposed to undergo a one electron, two proton minor equilibrium PCET reaction to form a $Co(OH)_2(OH_2)_4^{+}$ intermediate. It is known that the corresponding Co(III) hexaaquo complex has a pK_a of 2.9.[68] Inasmuch as deposition is performed at pH 7−9, it is reasonable to invoke a second deprotonation of this species. A surface equilibrium involving $MePO_3^{2-}$ dissociation accounts for the inverse first order dependence on MeP_i concentration. Since the cobaltate cluster most closely corresponds to an array of CoO(OH) units, a third deprotonation is expected and is in line with the overall inverse third order dependence of the experimental rate law. Whether this occurs from a species in solution or on the growing catalyst cluster is not known; in Figure 10, we show it to occur from a surface intermediate followed by rate-limiting binding of the $Co(OH)_2(OH_2)_4^{+}$ in solution to effect catalyst growth by one Co center (highlighted in pink in Figure 10). We note that alternative atomistic models for the deprotonation and buffer dissociation equilibria may be envisioned which are kinetically indistinguishable. Notwithstanding, the mechanistic sequence presented in Figure 10 can be repeated with adjacent surface sites to permit steady state growth in a fashion that is consistent with the experimental rate law.

The foregoing mechanism not only provides insight into the in situ catalyst formation but also sheds light on the self-repair mechanism of Co-OEC. Both formation and repair processes arise from the fact that, at > pH 7, the potentials necessary to sustain catalyst film formation and growth are below that required for water oxidation. Thus, upon application of a potential sufficient to generate oxygen, ample driving force exists to redeposit any Co in solution that may have leached from the film between catalyst operation cycles. Here, we find that the electrodeposition process exhibits an inverse third order dependence on proton activity, which is much greater than the inverse first order dependence observed for water oxidation catalysis mediated by Co-OEC catalyst films.[54] This disparity in proton order suggests that, as the pH is lowered, the potential necessary for catalyst formation will increase more quickly than the corresponding rise in potential required for water oxidation catalysis. This trend is shown graphically in Figure 11, where the potential versus pH profiles for water oxidation catalysis[54] and catalyst formation, both proceeding at the same activation controlled rate, are overlaid. While a sizable separation of 0.31 V is observed for the two processes at pH 8, extrapolation of the catalyst formation profile indicates that the two processes occur at the same potential at pH 5.2. Under the assumption that the rate law for catalyst formation remains unchanged down to pH 5.2, this crossover point provides a crude estimate of the pH regime in which in situ formation and catalyst self-repair remains operative. Indeed, direct measurement of the catalyst dissolution over a wide pH range (Figure 8) is qualitatively consistent with the prediction offered by Figure 11. Experimentally, no dissolution is detected at pH 6−7 whereas catalyst corrosion prevails at pH 5 and pH 4. In the catalyst corrosion experiments, complete catalyst dissolution would only give rise to a solution concentration of 50 μM Co^{2+}, approximately an order of magnitude lower than the 0.4 mM Co^{2+} concentration at which the data in Figure 11 were collected. Noting the first order Co^{2+} concentration dependence in the rate law, the more dilute conditions found in the
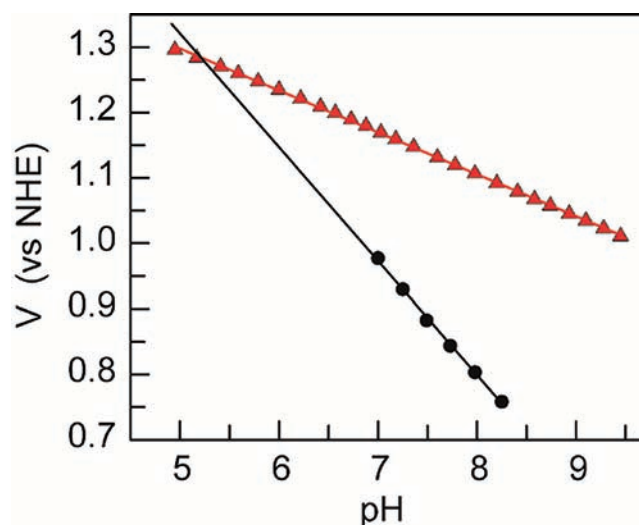
Figure 11. pH dependence of the potential for catalyst film formation (black ●) and oxygen evolution (red ▲) at j_{ac} = 30 μA/cm². Data for film formation were interpolated from Tafel plots in Figure S5. Data for oxygen evolution are reproduced from ref 54.

dissolution experiments would serve to increase the potential required for electrodeposition by ~60 mV and would cause the curves in Figure 11 to meet at ~pH 5.7, consistent with the experimental corrosion data. This predicted dependence of the pH regime of catalyst stability on Co^{2+} concentration also serves to explain the recent observation in the literature[69] that 1 mM Co^{2+} must be added to electrolyte solutions during catalyst operation to maintaining functional stability at pH 3.7. These observations indicate that control over the deposition potential through appropriate choice of electrolyte, pH, and Co^{2+} concentration is critical for enabling water oxidation and self-repair at intermediate pH.

■ CONCLUSION

A self-consistent model of the nucleation, growth, and repair processes of Co-OEC catalyst films has been constructed by using a combination of electrochemical, NMR, and AFM techniques. The nucleation of the catalyst proceeds by a progressive mechanism giving rise to islands, whose surface density can be controlled by modulating the electrodeposition potential and the duration of electrodeposition relative to the characteristic chronoamperometric peak. While future studies are needed to extend these findings to catalyst nucleation and growth on specific semiconductor substrates, these results provide a mechanistic foundation that may be leveraged to control the microstructure of Co-OEC functionalized photoanodes. The steady-state data for film growth point to a three proton, one electron PCET equilibrium prior to the rate limiting chemistry of Co association to the catalyst surface. The electrolyte assumes countering roles of facilitating rapid multiproton-coupled electron transfer while simultaneously inhibiting catalyst growth through surface adsorption. Together, the kinetic profiles of catalyst formation define the pH and electrolyte regimes of catalyst stability and self-repair, establishing a rational framework for future studies aimed at controlling the properties of the semiconductor−solution interface for the development of improved direct solar-to-fuels materials and devices.

■ ASSOCIATED CONTENT

Ⓢ Supporting Information

Full experimental details, additional nucleated growth traces, AFM images, Tafel plots, Koutecký−Levich plots, and NMR line broadening calibration curves. This material is available free of charge via the Internet at http://pubs.acs.org.

■ AUTHOR INFORMATION

Corresponding Author

nocera@mit.edu

Notes

The authors declare no competing financial interest.

■ ACKNOWLEDGMENTS

■ REFERENCES

(1) Nocera, D. G. *Inorg. Chem.* **2009**, *48*, 10001−10017.

(2) Lewis, N. S.; Nocera, D. G. *Proc. Natl. Acad. Sci. U.S.A.* **2006**, *103*, 15729−15735.

(3) Abbott, D. *Proc. IEEE* **2010**, *98*, 42−66.

(4) Cook, T. R.; Dogutan, D. K.; Reece, S. Y.; Surendranath, Y.; Teets, T. S.; Nocera, D. G. *Chem. Rev.* **2010**, *110*, 6474−6502.

(5) Cukier, R. I.; Nocera, D. G. *Annu. Rev. Phys. Chem.* **1998**, *49*, 337−369.

(6) Huynh, M. H. V.; Meyer, T. J. *Chem. Rev.* **2007**, *107*, 5004−5064.

(7) Hammes-Schiffer, S. *Acc. Chem. Res.* **2009**, *42*, 1881−1889.

(8) Siegbahn, P. E. M. *J. Am. Chem. Soc.* **2009**, *131*, 18238−18239.

(9) Concepcion, J. J.; Jurss, J. W.; Brennaman, M. K.; Hoertz, P. G.; Patrocinio, A. O. T.; Murakami Iha, N. Y.; Templeton, J. L.; Meyer, T. J. *Acc. Chem. Res.* **2009**, *42*, 1954−1965.

(10) Betley, T. A.; Wu, Q.; Van Voorhis, T.; Nocera, D. G. *Inorg. Chem.* **2008**, *47*, 1849−1861.

(11) Betley, T. A.; Surendranath, Y.; Childress, M. V.; Alliger, G. E.; Fu, R.; Cummins, C. C.; Nocera, D. G. *Phil. Trans. R. Soc., B* **2008**, *363*, 1293−1303.

(12) Dempsey, J. L.; Esswein, A. J.; Manke, D. R.; Rosenthal, J.; Soper, J. D.; Nocera, D. G. *Inorg. Chem.* **2005**, *44*, 6879−6892.

(13) Chang, C. J.; Chang, M. C. Y.; Damrauer, N. H.; Nocera, D. G. *Biophys. Biochim. Acta* **2004**, *1655*, 13−28.

(14) Surendranath, Y.; Nocera, D. G. *Prog. Inorg. Chem.* **2011**, *57*, 505−560.

(15) McDaniel, N. D.; Coughlin, F. J.; Tinker, L. L.; Bernhard, S. *J. Am. Chem. Soc.* **2008**, *130*, 210−217.

(16) Schley, N. D.; Blakemore, J. D.; Subbaiyan, N. K.; Incarvito, C. D.; D'Souza, F.; Crabtree, R. H.; Brudvig, G. W. *J. Am. Chem. Soc.* **2011**, *133*, 10473−10481.

(17) Blakemore, J. D.; Schley, N. D.; Balcells, D.; Hull, J. F.; Olack, G. W.; Incarvito, C. D.; Eisenstein, O.; Brudvig, G. W.; Crabtree, R. H. *J. Am. Chem. Soc.* **2010**, *132*, 16017−16029.

(18) Hull, J. F.; Balcells, D.; Blakemore, J. D.; Incarvito, C. D.; Eisenstein, O.; Brudvig, G. W.; Crabtree, R. H. *J. Am. Chem. Soc.* **2009**, *131*, 8730−8731.

(19) Grotjahn, D. B.; Brown, D. B.; Martin, J. K.; Marelius, D. C.; Abadjian, M.-C.; Tran, H. N.; Kalyuzhny, G.; Vecchio, K. S.; Specht, Z. G.; Cortes-Llamas, S. A.; Miranda-Soto, V.; van Niekerk, C.; Moore, C. E.; Rheingold, A. L. *J. Am. Chem. Soc.* **2011**, *133*, 19024−19027.

(20) Gao, Y.; Akermark, T.; Liu, J. H.; Sun, L. C.; Akermark, B. *J. Am. Chem. Soc.* **2009**, *131*, 8726−8727.

(21) Dogutan, D. K.; McGuire, R. Jr.; Shao-Horn, Y.; Nocera, D. G. *J. Am. Chem. Soc.* **2011**, *133*, 9178−9180.

(22) Brimblecombe, R.; Swiegers, G. F.; Dismukes, G. C.; Spiccia, L. *Angew. Chem., Int. Ed.* **2008**, *47*, 7335−7338.

(23) Hocking, R. K.; Brimblecombe, R.; Chang, L.-Y.; Singh, A.; Cheah, M. H.; Glover, C.; Casey, W. H.; Spiccia, L. *Nat. Chem.* **2011**, *3*, 461−466.

(24) Geletii, Y. V.; Botar, B.; Kögerler, P.; Hillesheim, D. A.; Musaev, D. G.; Hill, C. L. *Angew. Chem., Int. Ed.* **2008**, *47*, 3896−3899.

(25) Geletii, Y. V.; Besson, C.; Hou, Y.; Yin, Q.; Musaev, D. G.; Quiñonero, D.; Cao, R.; Hardcastle, K. I.; Proust, A.; Kögerler, P.; Hill, C. L. *J. Am. Chem. Soc.* **2009**, *131*, 17360−17370.

(26) Yin, Q.; Tan, J. M.; Besson, C.; Geletti, Y. V.; Musaev, D. G.; Kuznetsov, A. E.; Luo, Z.; Hardcastle, K. I.; Hill, C. L. *Science* **2010**, *328*, 342−345.

(27) Stracke, J. J.; Finke, R. G. *J. Am. Chem. Soc.* **2011**, *133*, 14872−14875.

(28) Chen, Z.; Concepcion, J. J.; Luo, H.; Hull, J. F.; Paul, A.; Meyer, T. J. *J. Am. Chem. Soc.* **2010**, *132*, 17670−17673.

(29) Concepcion, J. J.; Jurss, J. W.; Templeton, J. L.; Meyer, T. J. *J. Am. Chem. Soc.* **2008**, *130*, 16462−16463.

(30) Concepcion, J. J.; Jurss, J. W.; Norris, M. R.; Chen, Z.; Templeton, J. L.; Meyer, T. J. *Inorg. Chem.* **2010**, *49*, 1277−1279.

(31) Bernet, L.; Lalrempuia, R.; Ghattas, W.; Mueller-Bunz, H.; Vigara, L.; Llobet, A.; Albrecht, M. *Chem. Commun.* **2011**, *47*, 8058−8060.

(32) Romain, S.; Vigara, L.; Llobet, A. *Acc. Chem. Res.* **2009**, *42*, 1944−1953.

(33) Wasylenko, D. J.; Ganesamoorthy, C.; Henderson, M. A.; Koivisto, B. D.; Osthoff, H. D.; Berlinguette, C. P. *J. Am. Chem. Soc.* **2010**, *132*, 16094−16106.

(34) Wasylenko, D. J.; Ganesamoorthy, C.; Koivisto, B. D.; Henderson, M. A.; Berlinguette, C. P. *Inorg. Chem.* **2010**, *49*, 2202−2209.

(35) Nocera, D. G. *ChemSusChem* **2009**, *2*, 387−390.

(36) Kanan, M. W.; Nocera, D. G. *Science* **2008**, *321*, 1072−1075.

(37) Surendranath, Y.; Dincă, M.; Nocera, D. G. *J. Am. Chem. Soc.* **2009**, *131*, 2615−2620.

(38) Dincă, M.; Surendranath, Y.; Nocera, D. G. *Proc. Natl. Acad. Sci. U.S.A.* **2010**, *107*, 10337−10341.

(39) Esswein, A. J.; Surendranath, Y.; Reece, S. R.; Nocera, D. G. *Energy Environ. Sci.* **2011**, *4*, 499−504.

(40) Lutterman, D. A.; Surendranath, Y.; Nocera, D. G. *J. Am. Chem. Soc.* **2009**, *131*, 3838−3839.

(41) Kanan, M. W.; Surendranath, Y.; Nocera, D. G. *Chem. Soc. Rev.* **2009**, *38*, 109−114.

(42) Zhong, D. K.; Sun, J.; Inumaru, H.; Gamelin, D. R. *J. Am. Chem. Soc.* **2009**, *131*, 6086−6087.

(43) Zhong, D. K.; Gamelin, D. R. *J. Am. Chem. Soc.* **2010**, *132*, 4202−4207.

(44) Steinmiller, E. M. P.; Choi, K. S. *Proc. Natl. Acad. Sci. U.S.A.* **2009**, *106*, 20633−20636.

(45) Seabold, J. A.; Choi, K. S. *Chem. Mater.* **2011**, *23*, 1105−1112.

(46) Zhong, D. K.; Cornuz, M.; Sivula, K.; Grätzel, M.; Gamelin, D. R. *Energy Environ. Sci.* **2011**, *4*, 1759−1764.

(47) McDonald, K. J.; Choi, K.-S. *Chem. Mater.* **2011**, *23*, 1686−1693.

(48) Zhong, D. K.; Choi, S.; Gamelin, D. R. *J. Am. Chem. Soc.* **2011**, *133*, 18370−18377.

(49) Pijpers, J. J. H.; Winkler, M. T.; Surendranath, Y.; Buonassisi, T.; Nocera, D. G. *Proc. Natl. Acad. Sci. U.S.A.* **2011**, *108*, 10056−10061.

(50) Reece, S. Y.; Hamel, J. A.; Sung, K.; Jarvi, T. D.; Esswein, A. J.; Pijpers, J. J. H.; Nocera, D. G. *Science* **2011**, *334*, 645−648.

(51) Nocera, D. G. *Acc. Chem. Res.* **2012**, in press.

(52) Kay, A.; Cesar, I.; Grätzel, M. *J. Am. Chem. Soc.* **2006**, *128*, 15714−15721.

(53) Su, J.; Feng, X.; Sloppy, J. D.; Guo, L.; Grimes, C. A. *Nano Lett.* **2010**, *11*, 203−208.

(54) Surendranath, Y.; Kanan, M. W.; Nocera, D. G. *J. Am. Chem. Soc.* **2010**, *132*, 16501−16509.

(55) Bard, A. J.; Faulkner, L. R. *Electrochemical Methods: Fundamentals and Applications*; Wiley: New York, 2001; pp 340−344.

(56) Gileadi, E. *Electrode Kinetics for Chemists, Chemical Engineers, and Materials Scientists*; Wiley-VCH: New York, 1993; pp 127−184.

(57) Bard, A. J.; Faulkner, L. R. *Electrochemical Methods: Fundamentals and Applications*; Wiley: New York, 2001; Chapter 5.

(58) Scharifker, B.; Hills, G. *Electrochim. Acta* **1983**, *28*, 879−889.

(59) Zheng, M.; West, A. C. *J. Electrochem. Soc.* **2004**, *151*, C502−C507.

(60) Mirkin, M. V.; Nilov, A. P. *J. Electroanal. Chem.* **1990**, *283*, 35−51.

(61) Sluyters-Rehbach, M.; Wijenberg, J. H. O. J.; Bosco, E.; Sluyters, J. H. *J. Electroanal. Chem.* **1987**, *236*, 1−20.

(62) Bard, A. J.; Faulkner, L. R. *Electrochemical Methods: Fundamentals and Applications*; Wiley: New York, 2001; p 35.

(63) Kanan, M. W.; Yano, J.; Surendranath, Y.; Dincă, M.; Yachandra, V. K.; Nocera, D. G. *J. Am. Chem. Soc.* **2010**, *132*, 13692−13701.

(64) Haynes, W. M.; Lide, D. R. *CRC Handbook of Chemistry and Physics*, 91st ed., Internet Version; CRC Press: Boca Raton, FL, 2011; pp 8−21.

(65) Sigel, H.; Chen, D.; Corfu, N. A.; Gregan, F.; Holy, A.; Strasak, M. *Helv. Chim. Acta* **1992**, *75*, 2634−2656.

(66) Martell, A. E.; Smith, R. M.; Motekaitis, R. J. *Database 46: NIST Critically Selected Stability Constants of Metal Complexes, Version 8*; Texas A&M University: College Station, TX.

(67) Poltavets, V. V.; Croft, M.; Greenblatt, M. *Phys. Rev. B* **2006**, *74*, 125103/1−8.

(68) Sisley, M. J.; Jordan, R. B. *Inorg. Chem.* **2006**, *45*, 10758−10763.

(69) Gerken, J. B.; Landis, E. C.; Hamers, R. J.; Stahl, S. S. *ChemSusChem* **2010**, *3*, 1176−1179.